Materials Today Advances 23 (2024) 100524

Contents lists available at ScienceDirect

Materials Today Advances

journal homepage: www.sciencedirect.com/journal/materials-today-advances/

Not only a matter of disorder in I-WP minimal surface-based photonic networks: Diffusive structural color in *Sternotomis amabilis* longhorn beetles

Viola Bauernfeind [a,b], Vinodkumar Saranathan [c], Kenza Djeghdi [a,b], Elena Longo [d,1], Silja Flenner [d], Imke Greving [d], Ullrich Steiner [a,b], Bodo D. Wilts [b,e,*]

[a] Adolphe Merkle Institute, University of Fribourg, Chemin des Verdiers 4, 1700 Fribourg, Switzerland
[b] Swiss National Center for Competence in Research (NCCR) Bio-Inspired Materials, University of Fribourg, Chemin des Verdiers 4, 1700 Fribourg, Switzerland
[c] Division of Sciences, School of Interwoven Arts and Sciences, Krea University, Central Expressway 5655, Sri City, 517646 Andhra Pradesh, India
[d] Institute of Materials Physics, Helmholtz-Zentrum Hereon, Max-Planck-Str. 1, 21502 Geesthacht, Germany
[e] Department for Chemistry and Physics of Materials, University of Salzburg, Jakob-Haringer-Str. 2a, 5020 Salzburg, Austria

ARTICLE INFO

Dataset link: 10.5281/zenodo.7568053

Keywords:
Photonic crystals
Disorder
Diffusive structural color
Longhorn beetle

ABSTRACT

The diverse colors of longhorn beetles arise from either pigmentary absorption or interference of light with various photonic nanostructures. Variations in structure, order, and/or material composition give rise to diverse optical signals. Here, we investigated the colors of the longhorn beetle *Sternotomis amabilis sylvia* (Cerambycidae: Lamiinae). By combining optical microscopy and detailed bulk ultrastructural analysis of the colored scales that are the basis of the multicolored patterns of bluish-green and orange markings, we document polycrystalline networks based on the triply periodic minimal surface, Schoen's I-WP, in the bluish-green scales. In contrast, amorphous quasi-ordered networks are found in the orange scales. The optical signal from the photonic networks is further altered by absorbing pigments. Ridged, micrometer-sized protrusions diffuse reflected light and suppress iridescence in all scale types. We discuss the pivotal role that order and disorder play in these photonic structures and support our understanding of the function of the scale geometry with full-wave optical simulations. Detailed knowledge about visible light interactions within intricate mediums, such as those observed in beetle scales, is highly relevant to current challenges in the design and synthesis of photonic nanostructures operating in the visible regime.

1. Introduction

Insects, the most speciose group on Earth, feature a wide variety of color-producing mechanisms that are used in camouflage, thermoregulation and/or signaling [1–4]. Pigmentary colors are produced by chemical compounds that selectively absorb light and are observation-angle-independent [5]. In contrast, structural color results from the interference of light in materials that have periodic or quasiperiodic refractive index variations. Natural variations in refractive index occur most commonly in thin films [6–8], multilayers [6,9,10], diffraction gratings [11–13] or photonic crystals [3,14–19] and can lead to strong iridescence or angle dependence of optical signals, for example, in many butterflies, moths, bees, beetles and spiders [19–23]. The perceived optical signal often results from a combination of additive and subtractive mechanisms that combine structural and pigmentary coloration [21,24–26]. A profound understanding of many natural photonic structures increasingly requires an analysis going beyond the nanostructure to look at the role of order vs. disorder, interactions with pigments, and the interplay with the macroscopic geometry. Examples include the recent discovery of an ordered I-WP-like photonic network in a longhorn beetle and its amorphous counterpart in a closely related species [15,27]. Variations in the nature of periodicity, size, orientation, or composition within the same structure suggest previously unappreciated precise control mechanisms for order parameters within biophotonic structures [9,19,27–32]. Disorder in biophotonic structures generally alters the light scattering leading to non-iridescent or isotropic coloration [16,27,28,33,34] that are of great interest to optical physicists and engineers working in the burgeoning field of amorphous photonics [35,36].

The ecological relevance of gloss and iridescence for camouflage and signaling is well-studied [1,3,37–39]. While the functions of matte, non-iridescent optical signals are less well known [40], they could also support signaling by suppressing directionality or polarization dependence. In addition to directly altering the photonic nanostructures

* Corresponding author at: Department for Chemistry and Physics of Materials, University of Salzburg, Jakob-Haringer-Str. 2a, 5020 Salzburg, Austria.
E-mail address: bodo.wilts@plus.ac.at (B.D. Wilts).
[1] Current address: Elettra-Sincrotrone Trieste S.C.p.A., 34149 Basovizza (Trieste), Italy.

https://doi.org/10.1016/j.mtadv.2024.100524
Received 9 June 2024; Received in revised form 9 August 2024; Accepted 21 August 2024

that produce structural coloration, some species have evolved other means to suppress iridescence from photonic crystals. For instance, the scales of the Cattleheart butterfly, *Parides spp.*, contain either a polycrystalline gyroid-type photonic crystal slab or a perforated multilayer underlying a honeycomb-like layer that functions as a diffuser and scatters light in an angle-independent manner, resulting in a stable color appearance [41]. Similarly, the monkey beetle *Hoplia argentea* bears scales containing a multi-layered photonic structure covered by a layer of brush-like filaments. This layer diffuses incident and reflected light, thereby reducing the directionality of the optical signal, probably supporting camouflage [42].

Angle-independent coloration is widespread in longhorn beetles that often display colorful body patterns with hues ranging from blue to red. These beetles mainly feed on wood or roots (larval stage) [43–45] and typically have long antennae that can exceed the size of the body of the beetles. The coloration of many beetles is due to hair-like setae or elongated scales that adorn the elytron and body. These features can be filled with diverse photonic nanostructures, including chitinous opals, randomly packed spherical assemblies, or 3D photonic networks with varying degrees of translational order. Some beetles incorporate pigments into their composition [9,15,19,27,30]. Within the longhorn beetle subfamily Lamiinae [46], the Sternotomini [45] is the only tribe in which photonic networks based on triply periodic minimal surfaces (TPMS) have been reported, which makes them very interesting for understanding complex self-assembly mechanisms in nature [19,47–49]. Saranathan et al. proposed the presence of primitive or simple cubic networks that are based on Schwarz's *P* minimal surface in some *Sternotomis spp*. beetles based on synchrotron USAXS measurements and 2D scanning electron micrographs. However, in green scales of *Sternotomis callais*, Kobayashi et al. reported I-WP TPMS-like networks with body-centered cubic symmetry (bcc, "I" lent from the German "innenzentriert") and a unit cell resembling a wrapped package ("WP") which show polarization-dependent colors [15,50]. The authors also noted the peculiar shape of *Sternotomis callais* scales, comprising a vertically extended, ridge-bearing cortex. Bauernfeind et al. recently reported an amorphous photonic network with local I-WP character in *Sternotomis virescens* [27], where no such scale extensions were visible. To clarify the differing nanostructural diagnoses and to investigate the possible function of the particular scale geometry observed in some *Sternotomis* beetles, we investigate the origin of color in *Sternotomis amabilis sylvia* beetles using a combination of bulk nanostructural analyses, complemented by detailed optical measurements and electromagnetic modeling.

2. Results

Sternotomis amabilis sylvia (Hope, 1843) longhorn beetles are native to western and central Africa. A male specimen of *S. amabilis sylvia* with the characteristic long antennae is shown in Fig. 1a. The beetles measure about 25 mm in body length and display a colorful pattern of bright bluish-green (G) areas separated by black (B) stripes running across their body. Each wing bears one large central orange spot and a small posterior orange spot (O). When viewing the insect in daylight at normal and oblique angles, a minimal color change from green to turquoise was perceivable in the bluish-green areas (green for brevity), while orange patches did not change their appearance.

2.1. Optical characterization

Epi-illumination light microscopy revealed that in colored areas of the insect body, colored scales cover the otherwise black elytron. Bright-field micrographs in Fig. 1b,c show green and orange areas on the beetle wings with scales arranged parallel in tightly juxtaposed or reticulate structures along the insect's longitudinal axis (top to bottom, as in Fig. 1a). In the black areas, the elytron is mostly covered with black scales (see Figure S1a,b). The base is the widest part of the scales, which appears brighter than the more dull-colored, partially overlapping distal tip of the scales, which we call fin. The base of green scales is iridescent, while the base of orange scales appears matte. Individual scales in side-view (Fig. 1d,e) exhibit a spatulate profile. The scale base is about ~5 μm thick, flat at the bottom, slightly convex at the top, and extends vertically to form the about 30 μm to 45 μm high transparent fin, as marked by arrows in the inset of Fig. 1f. The colors originate only from one part of the 50 μm to 90 μm long scales, from the interior lumen (sketched in gray in the inset in Fig. 1f). Close inspection of the fins revealed two sets of chevron-shaped parallel ridges meeting centrally. These ridges are homologous to typical ridges seen on the surface of butterfly wing scales, given that scales in insects are homologs [51]. A detailed analysis of the scale geometry for all scale colors is provided in the Supplementary Information (Table S1).

We performed integrating sphere measurements to measure the wavelength-resolved reflectivity of the color patches on the insect. The reflectivity spectra of green and orange areas, visible in Fig. 1f, showed a single peak differing in hue and saturation. Spectra of green areas showed a narrow reflectance band with a peak intensity of about 0.2 at (543 ± 7) nm with a FWHM of (91 ± 2) nm (green line and shaded area in Fig. 1f, number of averaged measurements $N = 5$), as expected for structural colors generated by a photonic crystal [17,52]. Spectra from orange areas with an averaged reflectivity of about 0.25 at (696 ± 17) nm had a broader band of about (321 ± 9) nm FWHM (orange line in Fig. 1f, $N = 5$). Black regions were too small to be reliably measured with our integrating sphere setup due to the finite spot size of about 5 mm.

For analysis of the reflection and transmission properties of individual scales, we used a microspectrophotometer (MSP) setup (see Materials and methods). Reflectance spectra recorded at the base and fin (see Figure S2c) of individual, pristine scales ($N = 30$) on the insect are shown in Figure S2. Minimal differences between the two measurement positions were observed for all scale colors, even though the base of green scales reflected more brightly than the fins. The peak position at ~540 nm was similar for green scales. In contrast, the peak positions for orange scales from the base and tip were situated at ~670 nm and ~710 nm, respectively. The MSP reflectance spectra closely resembled the spectra obtained from integrating sphere measurements for both scale colors but differed in the overall intensities due to the limited numerical aperture of the objective. Black scales reflected less than 10% of the incoming light (see Supplementary Information).

To investigate whether the origin of the scale colors is purely structural, we immersed the scales in a refractive index-matching oil with a refractive index of $n = 1.55$ close to that of chitin [53,54] and compared the transmitted intensity to the transmittance of scales in air (see Supplementary Information, Figure S3). The obtained absorbance spectra showed that both scale types contain pigments that absorb the strongest at short wavelengths (Supplementary Information, Figure S4). The spectra are reminiscent of melanin in green scales and further indicate the presence of a different narrow-band absorbing pigment in the orange scales. Black scales were highly pigmented and transmitted less than 60% of the incoming light upon oil immersion. These measurements further allowed us to calculate the complex refractive index of the chitinous, pigmented cuticle material that makes up the green and orange scales (see Supplementary Information, Figure S4).

To investigate whether the ridge-decorated fins influenced the scattering behavior of the green and orange scales, we performed back-focal plane (*k*-space) imaging [55,56]. The scattering behavior was measured on upright scales mounted on carbon tape for narrow-angle illumination (parallel arrows in Fig. 2, half-opening angle of 15°) and wide-angle illumination (concentric arrows in Fig. 2, half-opening angle of 64°) with a constant spot size (see Materials and methods). Micrographs of scales under narrow- and wide-angle illumination are shown in Figure S2d,e. Narrow-angle illumination of green scale bases produced specular, predominantly green reflections (Fig. 2b, top-left) and a gray band across all scattering angles extending about normal to the longitudinal scale axis, the specular reflection off of the convex cortex surface (see

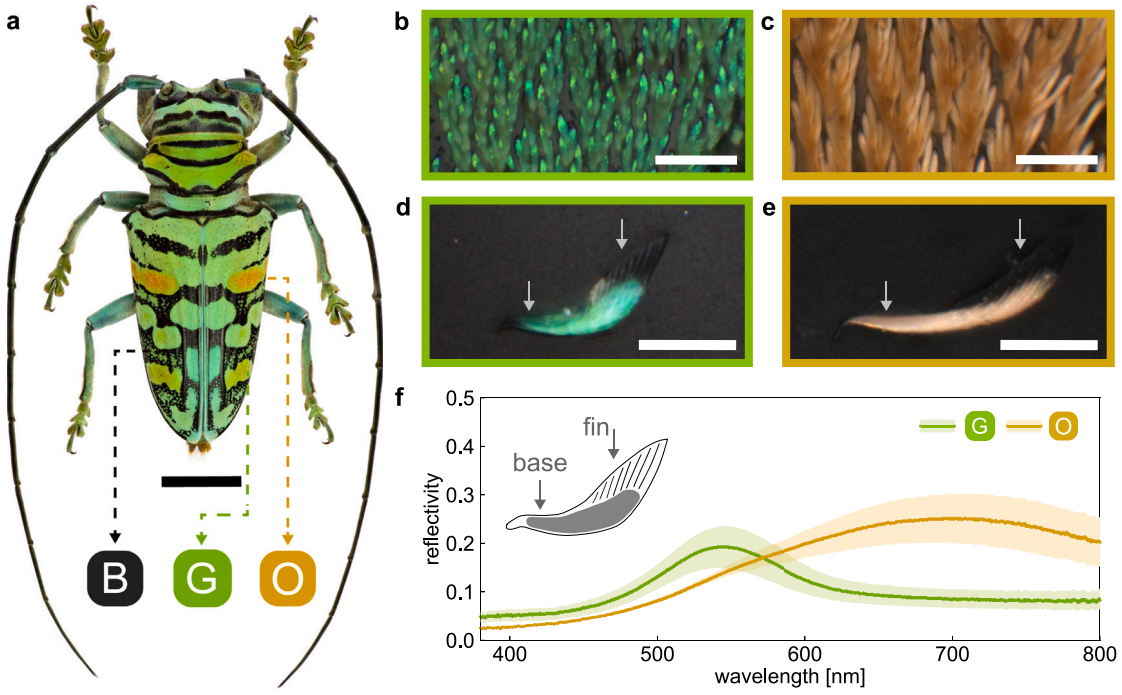

Fig. 1. Vividly colored scales create bluish-green, orange, and black patterns in *Sternotomis amabilis sylvia* longhorn beetles. **a** Photograph of a male *S. amabilis sylvia* specimen, reproduced with permission of S. Kakunin. **b,c** Bright-field microscopy images show the arrangement of green (b) and orange (c) scales on the black elytron. **d,e** Bright-field micrographs of an individual green (d) and orange (e) scale on carbon tape in side-view. Arrows indicate the base and fin. **f** Averaged reflectivity spectra ($N = 5$, continuous line) of colored patches on the insect measured with an integrating sphere. Shaded regions indicate the standard deviation. Inset: Sketch of the scale geometry in side view. Scale bars a: 0.5 cm, b,c: 100 µm, d,e: 50 µm. (For interpretation of the references to color in this figure legend, the reader is referred to the web version of this article.)

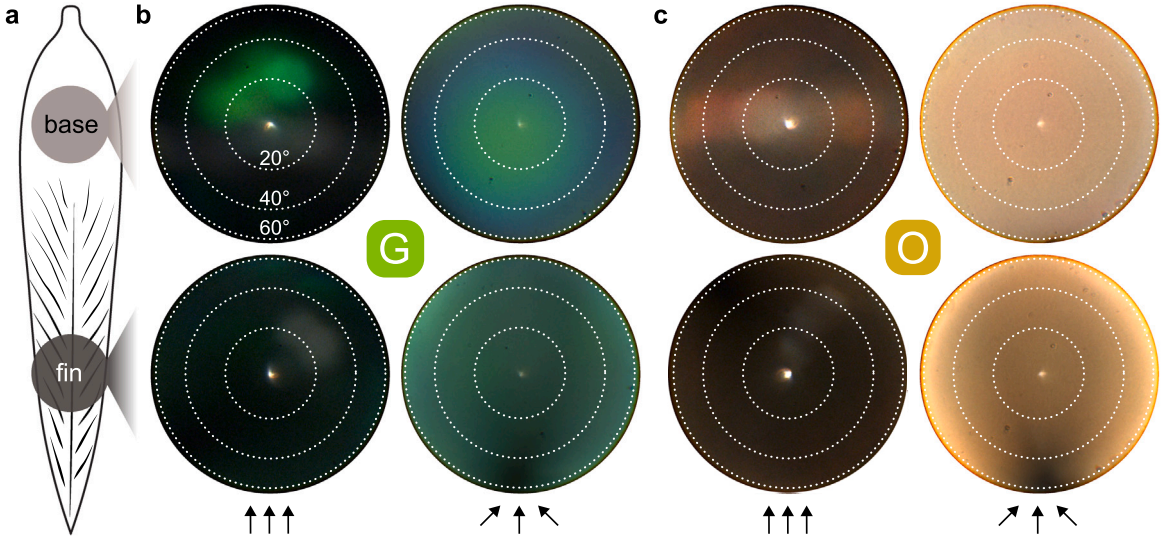

Fig. 2. Scattering behavior of the scale base and fin measured with *k*-space imaging. **a** Sketch of a scale in top view showing the unstructured base and ridged fin. The measurement spots at the "base" and "fin" are drawn as light- and dark-gray circles, respectively. **b,c** *k*-space images recorded at the base (top row) and fin (bottom row) of green (b) and orange (c) scales. The angular distribution of the illumination is indicated by parallel (narrow) and concentric (wide) arrows at the bottom, which apply to the respective column above. Dotted circles of increasing radius indicate scattering angles of 20°, 40°, and 60°. (For interpretation of the references to color in this figure legend, the reader is referred to the web version of this article.)

Supplementary Information, Figure S11). Wide-angle illumination of the base resulted in a gradual color change from bright green to blue for increasing scattering angles (Fig. 2b, top-right), characteristic of iridescence.

The fin of green scales scattered light diffusely regardless of the illumination settings (Fig. 2b, bottom). For wide-angle illumination, a homogeneous green color from the fin contrasted with the iridescence observed for the scale base. The first deviated from an even distribution by a dark wedge typically oriented parallel to the ridged tip, suggesting a shadowing effect along the scale axis.

The base of orange scales scattered light of narrow-angle distribution into a band of orange to gray color (Fig. 2c, top-left), and strong specular reflections were absent. A homogeneous beige was observed for all directions and scattering angles up to 64° for wide-angle illumination. Illuminating the fin of orange scales with narrow- and wide-angular spread resulted in mostly homogeneous beige to orange hues of different intensities and the above-discussed shadowing effect.

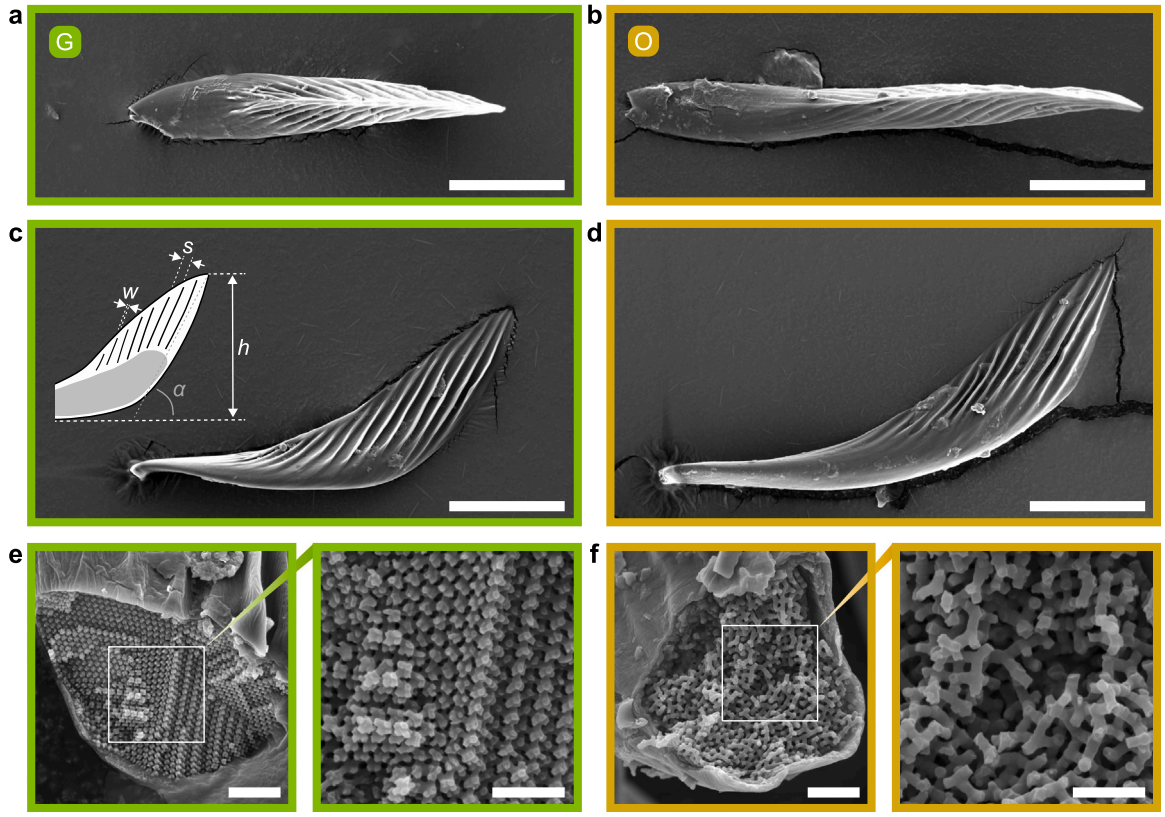

Fig. 3. Scanning electron microscopy images reveal the ultrastructure of *Sternotomis amabilis sylvia* beetle scales. **a,b** Top-view SEM images of a green (a) and orange (b) scale show the unstructured base and ridged fin. **c,d** Side-view SEM images of a green (c) and orange (d) scale illustrate the scale geometry. Inset: Sketch of the ridged fin including the geometrical parameters fin elevation h, fin angle α, ridge width w, and ridge spacing s, as defined in the Supplementary Information and Figure S8. **e,f** SEM images of fractured green (e) and orange (f) scales. Regions in white inset boxes are displayed at higher magnification on the right, where a periodic structure is found in green scales and a disordered network in orange scales. Scale bars: a–d 20 µm, e,f 2 µm, insets in e,f 1 µm. (For interpretation of the references to color in this figure legend, the reader is referred to the web version of this article.)

The angle-dependent light scattering at the base of green scales contrasted the largely angle-independent scattering at their fin, suggesting a diffusing effect of the ridged fin, which eradicates any iridescence. For orange scales, we found the diffusing effect of the ridged fin to have minimal influence on the scattering behavior and thus concluded that the angle-independence originates from a structurally isotropic scale interior.

2.2. Structural analysis

To further investigate the structural origin of light scattering from the differently colored scales, we performed ultrastructural scale analyses using electron microscopy, slice-and-view volume reconstruction, synchrotron ultra-small-angle X-ray scattering (USAXS), and synchrotron nanotomography. Scanning electron microscopy (SEM) images in Fig. 3a–d show complex-shaped single scales on carbon tape; the arrangement of pristine scales on the elytron is shown in the Supplementary Information (Figure S5). The spatulate scales feature an oblate base, (3.5 ± 0.5) µm and (4.9 ± 0.6) µm thick in green and orange scales ($N = 15$), respectively. The base extends vertically into the ridged fin, reaching an average projected scale length of (55 ± 6) µm (green scales) and (84 ± 6) µm (orange scales, $N = 15$). The Supplementary Information (Figure S6) discusses the ultrastructure of black scales.

Motivated by the different scattering behavior of different scale areas, two aspects of the scale ultrastructure were investigated in detail: (i) the fin geometry and (ii) the internal structure of the scales. To describe the complex fin geometry (see Figure S7, Supplementary Information), we defined several geometrical parameters accessible from top-view SEM images and cross-sectional images using focused ion beam milling (FIB): (1) the fin elevation h and (2) the fin angle α relative to the elytron base, (3) the ridge width w, (4) the ridge depth d and (5) the ridge spacing s (see inset in Fig. 3c, Figure S8 and Table S1). The Supplementary Information provides a full description of the scale geometry of all scale types.

The fins of green and orange scales showed minor differences in fin elevation ((32 ± 5) µm and (44 ± 5) µm, respectively), fin angle ($(64 \pm 8)°$ and $(63 \pm 6)°$), ridge spacing ((1.5 ± 0.3) µm and (1.8 ± 0.5) µm) and ridge depth ((1.2 ± 0.4) µm and (1.1 ± 0.4) µm, $N = 15$). Ridges in green scales, (370 ± 150) nm wide, were about half as wide as those in orange scales ((680 ± 200) nm), while black scales featured only weakly developed ridges (see Supplementary Information Figure S7). High-magnification SEM images of the fins also showed a fishbone grating with ~100 nm spacing (see Figure S7), similar to what has been reported in other Sternotomini [15,27].

Fractured scales offered insight into the internal structure of the scales, shown in Fig. 3e,f. Green scales exhibited an ordered three-dimensional network and motifs similar to the TPMS-like structures reported in other *Sternotomis* beetles [15,19,50]. Orange scales contained a more disordered network (Fig. 3f), where many connections appeared to be 3- or 4-fold coordinated. Interestingly, even black scales contained visibly disordered networks (see Figure S6).

2.2.1. Synchrotron ultra-small-angle X-ray scattering and nanotomography

We obtained bulk structural information about the photonic networks from synchrotron ultra-small-angle X-ray scattering (USAXS) assays of entire scales. Representative two-dimensional diffraction patterns of a green, orange, and black scale are presented in Fig. 4c–e. Azimuthally-smeared spots on concentric rings provide evidence of

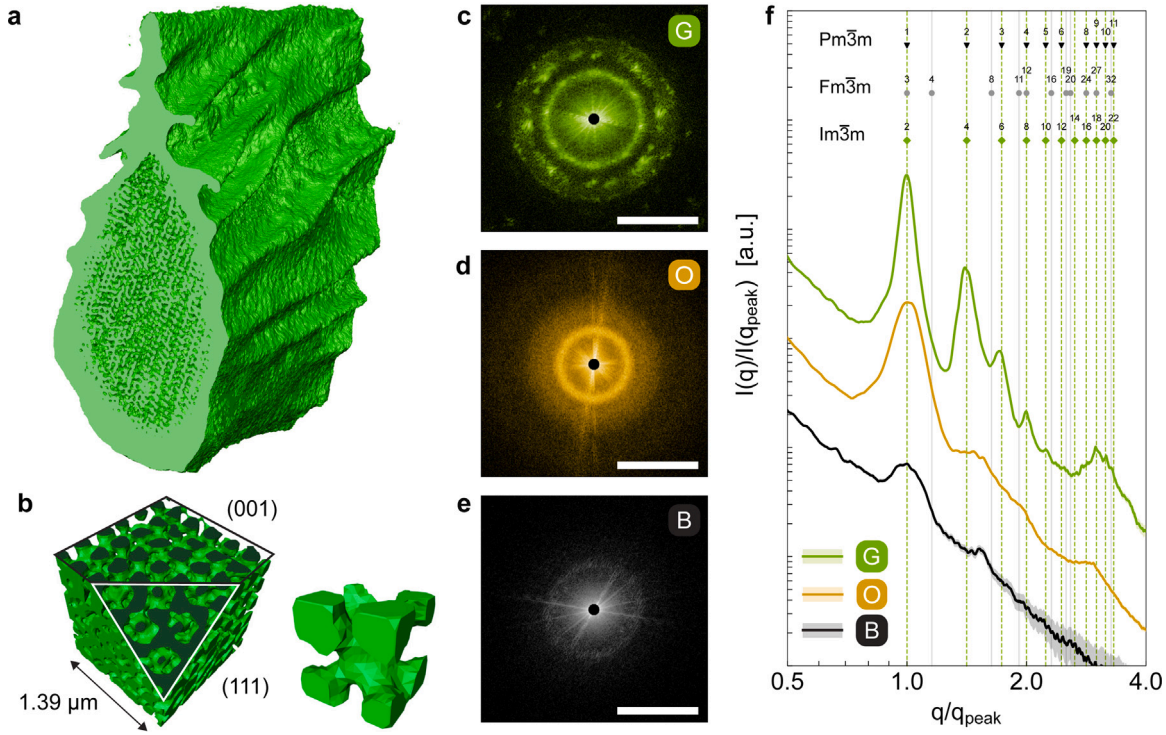

Fig. 4. USAXS assays of *Sternotomis amabilis sylvia* beetle scales and a 3D network reconstruction obtained from synchrotron nanotomography. **a** Reconstructed part of a green scale toward the fin with the cross-section showing the photonic crystal inside the scale. **b** Left: Reconstructed photonic network visible in (a) showing the (001) and (111) planes framed in black and white, respectively. Right: A unit cell of the reconstructed volume with unit cell parameter (245 ± 21) nm that, despite visible artifacts, still resembles the I-WP unit cell [15].**c,d,e** False-colored, logarithmic 2D scattering intensity of a green (c), orange (d) and black (e) scale. Scale bars $0.05\,\mathrm{nm}^{-1}$. **f** Azimuthally integrated scattering intensity, normalized to the peak position q/q_{peak} and to the peak intensity of the first peak. The curves are offset in intensity for clarity. (For interpretation of the references to color in this figure legend, the reader is referred to the web version of this article.)

polycrystallinity in the ordered networks of the green scale (Fig. 4c). For the orange and weakly scattering black scale, ring features in the 2D patterns in Fig. 4d,e document the structural isotropy of the corresponding networks [19]. However, the shape of the ring in the pattern from the black scale is ellipsoidal rather than circular suggesting some degree of anisotropy.

For structural diagnoses via crystallographic indexing, the 2D patterns were azimuthally integrated and plotted as normalized scattering curves scaled with q/q_{peak} in Fig. 4f. The curves for the orange and black scales showed a few broad higher-order peaks, while multiple sharp Bragg peaks were observed for the green scale. The primary peaks for the green (G), orange (O) and black scale (B) are at $q_{\mathrm{peak,G}} = 0.0291\,\mathrm{nm}^{-1}$, $q_{\mathrm{peak,O}} = 0.0209\,\mathrm{nm}^{-1}$ and $q_{\mathrm{peak,B}} = 0.0264\,\mathrm{nm}^{-1}$, respectively, which correspond to average correlation lengths of $d_{\mathrm{peak,G}} = 216\,\mathrm{nm}$, $d_{\mathrm{peak,O}} = 301\,\mathrm{nm}$ and $d_{\mathrm{peak,B}} = 238\,\mathrm{nm}$ (see Supplementary Information).

For the quasi-ordered network, the correlation length of $d_{\mathrm{peak,O}} = 302\,\mathrm{nm}$ accurately reproduced the average strut length of (300 ± 30) nm obtained from slice-and-view volumetric data discussed in the next section. A symmetry assignment was only practical for the ordered network in the green scale where the peaks were compared to expected peak positions for the alternative space groups $Pm\bar{3}m$, $Fm\bar{3}m$ and $Im\bar{3}m$. While the position of the second peak excluded an assignment to $Fm\bar{3}m$, based on the presence of the peak at $q/q_{\mathrm{peak}} = \sqrt{2}$, an assignment to either $Pm\bar{3}m$ or $Im\bar{3}m$ is valid. Further, the presence of the $\sqrt{7}$ peak is not clear enough to positively identify the ordered network as $Im\bar{3}m$.

According to Bragg's law, the first allowed peak for $Im\bar{3}m$ corresponds to the ⟨110⟩ reflection, while it is the ⟨100⟩ for $Pm\bar{3}m$, with respective lattice parameters of $\sqrt{2} \times d_{\mathrm{peak,G}}$ and $1 \times d_{\mathrm{peak,G}}$. Based on the measurement of unit cell parameter as (300 ± 10) nm from the roughly ⟨100⟩ oriented domains in the SEM data Figure S10e, we can exclude the $Pm\bar{3}m$ assignment. However, it is not possible to distinguish between alternative TPMS-based topologies all with the $Im\bar{3}m$ space group symmetry, specifically, plumber's nightmare, I-WP, or Neovius surfaces based solely on the obtained USAXS [57] or 2D-EM data [18]. The relative intensities of higher order USAXS peaks can be informative in this regard, although this is complicated when they are weak or get overlapped by peaks from multiple domains in the azimuthal or radial directions [57].

Despite its limitations, USAXS can provide quantitative information on the extent of order in networks by calculating the spatial coherence length $\zeta = 2\pi/\Delta q$ that describes the average size of the crystalline domains [58]. To determine the average domain size in the three scale types, we fitted the background and primary peak of the USAXS curves with Porod's law and a Lorentzian peak (see Supplementary Information). The ordered network in the green scale had crystalline domains of average size $4.0\,\mu\mathrm{m}$ that contrasted smaller calculated domains in orange ($2.4\,\mu\mathrm{m}$) and black scales ($0.8\,\mu\mathrm{m}$). While the latter two were not measurable from SEM data, the first matches the domain size measured from SEM images (see Supplementary Information, Table S1).

To resolve the ambiguity in 2D scattering of the various TPMS-based topologies with $Im\bar{3}m$ space group, we obtained volumetric data of a green and orange scale using synchrotron nanotomography. Fig. 4a shows the reconstructed volume from the distal part of a green scale. For the orange scale, disordered patterns were observed in the projections with a few selected projections shown in the Supplementary Information (Figure S9). A qualitative assignment to the I-WP-related structure was possible for the ordered network in the green scale based on the shape of the extracted unit cells and cross-sectional patterns (see Fig. 4b, compare Kobayashi et al.). The real space correlation length of $d_{\mathrm{peak,G}} = 216\,\mathrm{nm}$ therefore differed from the strut length L_{G}, measured along the (half) diagonal of the unit cell (along ⟨111⟩) [15]. With the strut length thus defined as $L_{\mathrm{G}} = \frac{\sqrt{3}}{2}a$ and the unit cell length $a = 305\,\mathrm{nm}$ calculated from $a = \sqrt{2}d_{\mathrm{peak,G}}$, $L_{\mathrm{G}} = 264\,\mathrm{nm}$ is obtained.

Given the relatively unambiguous identification of the ordered photonic networks as I-WP-like structure ($Im\bar{3}m$) based on nanotomography, we emphasize that reciprocal space USAXS as a standalone analysis appears unsuitable for space group assignment of complex TPMS-based cubic networks in the absence of corresponding volumetric real-space data. The presented nanotomography data could also serve as a basis for a detailed network analysis using skeletonization, but the comparably large voxel size significantly affected the reliability of the results. We, therefore, used a focused ion beam slice-and-view system to obtain an in-depth understanding of the local network characteristics in real space. Unfortunately, these systems typically have a volume restriction to a few tens of cubic microns, thus trading statistics for resolution.

2.2.2. Focused ion beam slice-and-view tomography

To complement the qualitative structural insights from 2D SEM images and support our USAXS diagnosis, we investigated the photonic networks using focused ion beam (FIB) milling and, in the first step, obtained serial cross-sections of intact scales. As seen in Figure S10, only the scale lumen that appeared colored in light microscopy contained photonic networks (compare Fig. 1), not the ridged fin. The cross-sections further allowed measuring the domain size in green scales and the thickness of the cortex enclosing the photonic networks at the scale base (see Table S1).

For quantitative network analysis, we performed slice-and-view (FIB-SEM) tomography to obtain volumetric data that were artifact-corrected following established protocols (see Materials and Methods, [27,28]). The analyzed subvolumes of $3 \times 3 \times 3\,\mu m^3$ are shown in Fig. 5a,c with the top surface oriented face-up as in the actual scale. The networks with volume fractions ~ 48% (green) and ~ 40% (orange) differed in the observed cut-plane motifs, which were periodic for the green scale (Fig. 5a,b) and disordered for the orange scales (Fig. 5c,d).

How can we ascertain whether the periodic network in green scales is an I-WP TPMS-based solid network as described in the scales of the related species, *S. callais*? First, we qualitatively compared the observed cut-face motifs in Fig. 5b with cross-sections of the I-WP TPMS-like structure in *S. callais* scales [15]. The upward-facing pattern of elongated ovals in Fig. 5b (center, white ovals) locally matched the (110) plane in the I-WP-based network. The pattern of circles and concentric dots on the cube's side (black frame) fits the (111) plane of the I-WP-based network [15].

Secondly, to quantitatively describe the geometry of the network, we skeletonized the networks. We then analyzed the resulting skeleton of vertices and struts, visible in Fig. 5e, g, with respect to (1) the strut length L, (2) the coordination number CN defined as the number of struts connected by one vertex, and (3) the bond angle β between struts connected by the same vertex. The strut length distributions in Fig. 5j show that struts in the green scale with average length $L_G = (255 \pm 22)\,nm$ ($N = 4917$), supporting the result obtained from USAXS, were shorter than struts in the orange scale with $L_O = (300 \pm 30)\,nm$ ($N = 1610$). Based on the strut length variation in the latter, the network in orange scales is hereafter called quasi-ordered.

To compare the reconstructed networks with known crystal structures, we evaluated their connectivity via the average coordination number. The periodic network in green scales has mostly 8-connected vertices (see Fig. 5i), with an average coordination number $CN_G = (7.3 \pm 2.9)$. This is demonstrated in the unit cell in Fig. 5f. The high standard deviation in the data was likely due to several structural defects in the reconstructed volume (see Fig. 5a,b,e). The quasi-ordered network in orange scales with few visible defects has an average coordination number of $CN_O = (4.9 \pm 0.9)$. A selected subunit is shown in Fig. 5h.

The bond angle distributions in Fig. 5k revealed further differences between the two networks. The angle distribution of the periodic network peaks at ~70°, ~110°, and ~175° ($N = 32775$). The first two peaks coincided with values expected for the I-WP structure (70.5°, 109.5°) (see [27], Supplementary Information), while the third peak, expected at 180°, was shifted to smaller angles. The quasi-ordered network showed an asymmetric distribution of bond angles with a peak at 87° ($N = 5808$) and a shoulder toward 170°, similar in shape to the bond angle distribution in the I-WP-like amorphous photonic networks in *Sternotomis virescens* [27].

The visual characteristics and statistical structural examination of the skeletonized networks align with the identification of a polycrystalline I-WP-like network in the green scales [15,27,50]. The quasi-ordered network in orange scales differed from the ordered I-WP-like structure in appearance and connectivity. Clearly, an assignment to the 3-connected gyroid-like networks [14,34,49,59] or 4-connected diamond-like structures [3,28,34,60,61] was precluded by the mismatch in coordination number. A concordance with the Schwarz's P surface [19,62], characterized by a coordination number of 6 and bond angles of 90° and 180° similarly appears unlikely. Moreover, photonic networks with I-WP character seem prevalent among Sternotomini [15,27] and reports of one insect genus with two different space groups are scarce [19]. We, therefore, identify I-WP-like networks in scales of *Sternotomis amabilis sylvia* with varying amounts of structural disorder, with the lower coordination number likely caused by a relatively higher amount of disorder [15,27].

2.3. Full-wave optical simulations

Finally, to examine the interplay of the scattering from photonic networks with complex macroscopic features such as the cortex and ridges and understand the origin of the angle-independent colors, we performed full-wave optical simulations using the finite-difference time-domain (FDTD) method. Simulations were performed in three dimensions (3D) on (i) the photonic networks and (ii) models of the scale cortex, oblate at the base and folded at the scale fin (simulated in two dimensions, 2D). Fig. 6 summarizes the simulation results.

We simulated the network reflectivity along different orientations to test for orientation dependence of the photonic networks. While the quasi-ordered network reflected about 10 to 20% between 650 nm to 750 nm along all directions, we observed more distinct variations only for the I-WP-like network (see Fig. 6a,b). It reflected up to 40% around 510 nm for orientations close to ⟨110⟩ (direction (1), (2), (3), (5), compare inset of Fig. 6b). Variations in the peak intensity for equivalent directions ((1), (2), (3), (5)) likely resulted from the domain misalignment with the ⟨110⟩ orientation and scattering at network defects (see Fig. 5a,b,e). When illuminated along ⟨111⟩ ((4), (6) in Fig. 6a), an almost constant reflectivity below 10% was obtained. No photonic band gap is expected along the ⟨111⟩ (P) direction for a perfect I-WP-type photonic crystal [50], consistent with our simulations. The observed non-zero reflectivity was likely related to surface reflections and scattering from defects. Overall, the orientation-dependent simulated reflectivity of the reconstructed I-WP-like network, therefore, agreed with the calculated band structure of the I-WP structure reported earlier by Ohnuki et al..

We examined the scattering behavior of the different networks with simulated scatterograms along the scale normal, (1) in Fig. 6b, for 0° horizontal polarization. As visible from the scatterogram in Fig. 6a (inset), the reconstructed I-WP-like domain preferentially scattered turquoise light into a spot at about 25°. This observation was consistent with the experimental specular reflections at the base of green scales for narrow-angle illumination. Further, it allowed estimating a relative tilt angle of 12.5° between the ⟨110⟩ direction and axis of the reconstructed domain. In contrast to the normal illumination in the simulation, omnidirectional ambient light will broaden the specular reflection toward a gradual color change at higher scattering angles per the photonic band structure [50].

The simulated scatterogram for the quasi-ordered network in Fig. 6b displayed dull green, yellow, and red spots distributed with little angle

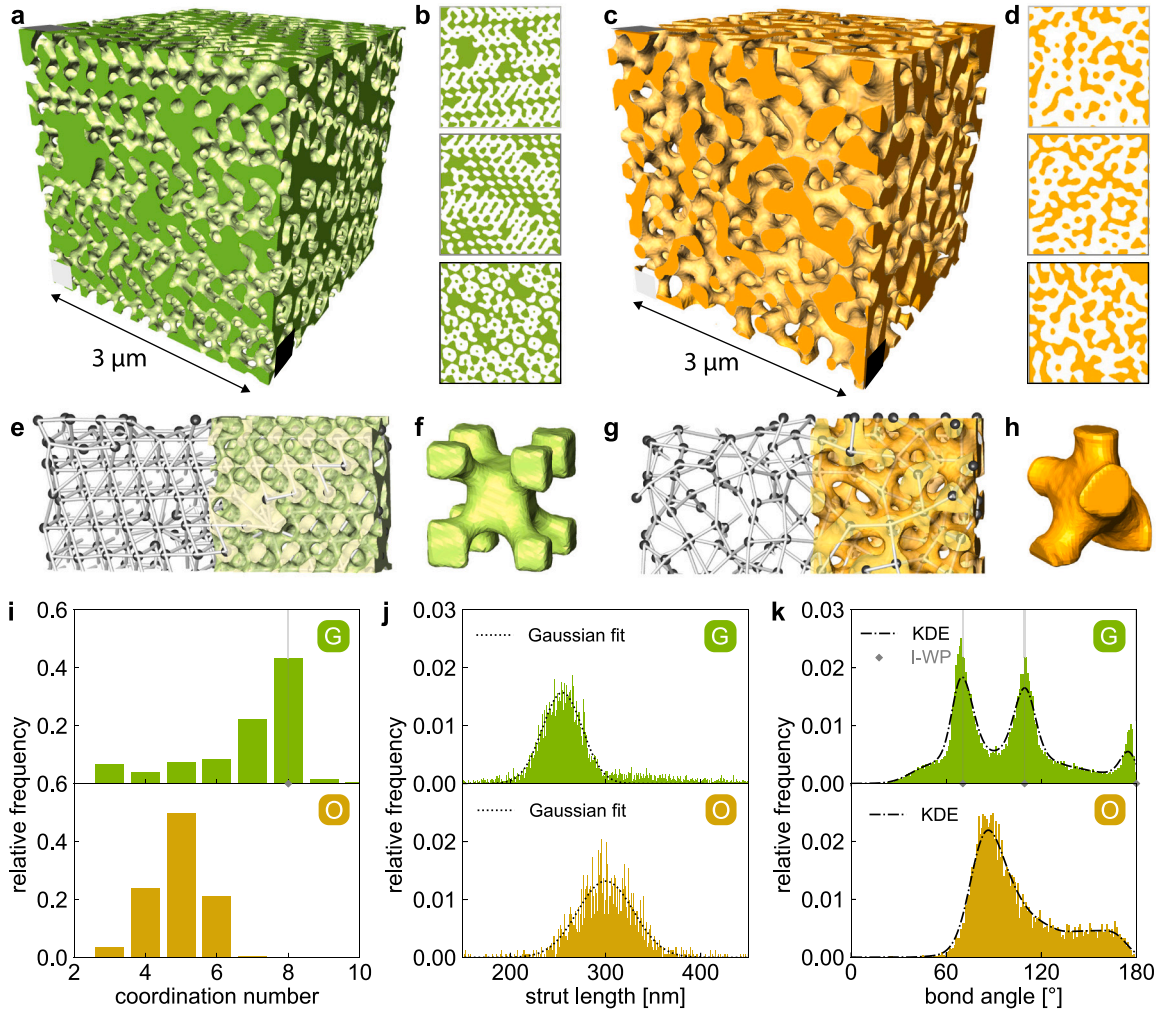

Fig. 5. 3D reconstructions of the photonic networks in green and orange scales using FIB slice-and-view tomography. **a,c** Perspective view of the reconstructed networks in a green (a) and orange scale (c). Light gray, dark gray and black squares indicate cross-section orientations. **b,d** Cross-sections of the volumes in the *xy* plane, *xz* plane (cut-face), and *yz* plane framed by light gray, dark gray, and black markers, respectively. **e,g** Sections of the skeletonized networks in the periodic network (e, green scale) and quasi-ordered network (g, orange scale). Black spheres represent vertices, white tubes struts. **f** Unit cell of the periodic network in a green scale. **h** A representative subunit with a five-fold coordination number extracted from the quasi-ordered network in an orange scale. **i,j,k** Graphs i–k show the distributions of **i** the vertex coordination number, **j** strut length, and **k** bond angles in the green (top, G) and orange scale (bottom, O). Dotted lines indicate Gaussian fits to the distributions, and dash-dotted lines represent Gaussian kernel density estimations (KDE). Gray lines and diamonds indicate expected values for the I-WP structure (compare [27]). (For interpretation of the references to color in this figure legend, the reader is referred to the web version of this article.)

dependence. The simulated pattern approximated the brown background in the experimental *k*-space image (compare Fig. 2) but did not capture the orange-gray band because the simulation neglected the convex cortex, as discussed below. While the simulated scatterogram based on normal incidence plane wave illumination was also not directly comparable to the appearance of the scales, the observed colors still matched those observed in light microscopy images of individual scales under narrow-angle illumination as seen in Figure S2d (bottom). For ambient illumination, one can expect a smearing out of the colored spots and, hence, an angle-independent beige or brown coloration, matching the experimental result.

To understand the optical role of the ridged distal cortex structure, a second set of simulations investigated the scattering behavior of the cortex enclosing the photonic networks, oblate at the base, and folded into a series of ridges at the fin. Cortex models were illuminated with (1) a plane wave from above and (2) a Gaussian beam from below to mimic the light reflected by the photonic network in the scale lumen, as sketched in Fig. 6c.

The model of the oblate cortex at the scale base acted as a convex-concave distributive lens for top illumination with a plane wave and produced a green-gray reflection band in the simulated scatterogram in Figure S11, matching the observed gray reflection band in experimental *k*-space images.

We explored the 2D scattering behavior of a triangular model with ridges (see Materials and methods) and a featureless triangular prism of equal volume, shown in Fig. 6c. To test for wavelength-selective scattering, we extracted 2D far-field scattering intensity distributions for wavelengths ranging from the ultraviolet-visible to the near infrared region. The far-field intensity distributions in Fig. 6d share a logarithmic intensity scale and highlight polarization-independent differences in scattering between the plain triangular prism and the ridge-bearing model (compare Figure S12a,b). The triangular prism caused minimal reflection when illuminated by plane waves. In contrast, the ridge-bearing structure scattered the light significantly, exhibiting little dependence on wavelength in the visible spectrum (see Figure S12c), thus demonstrating a diffusive function for incoming light. To also understand the interplay of the ridges with the light reflected by the photonic network in the scale lumen, we compared in-plane power distributions of both models for a single wavelength, $\lambda = 509\,\mathrm{nm}$, dominantly reflected by the I-WP-like network in green scales. The logarithmically-scaled power distributions in Fig. 6e illustrate that the plain prism (left) focused light from below the structure at the top

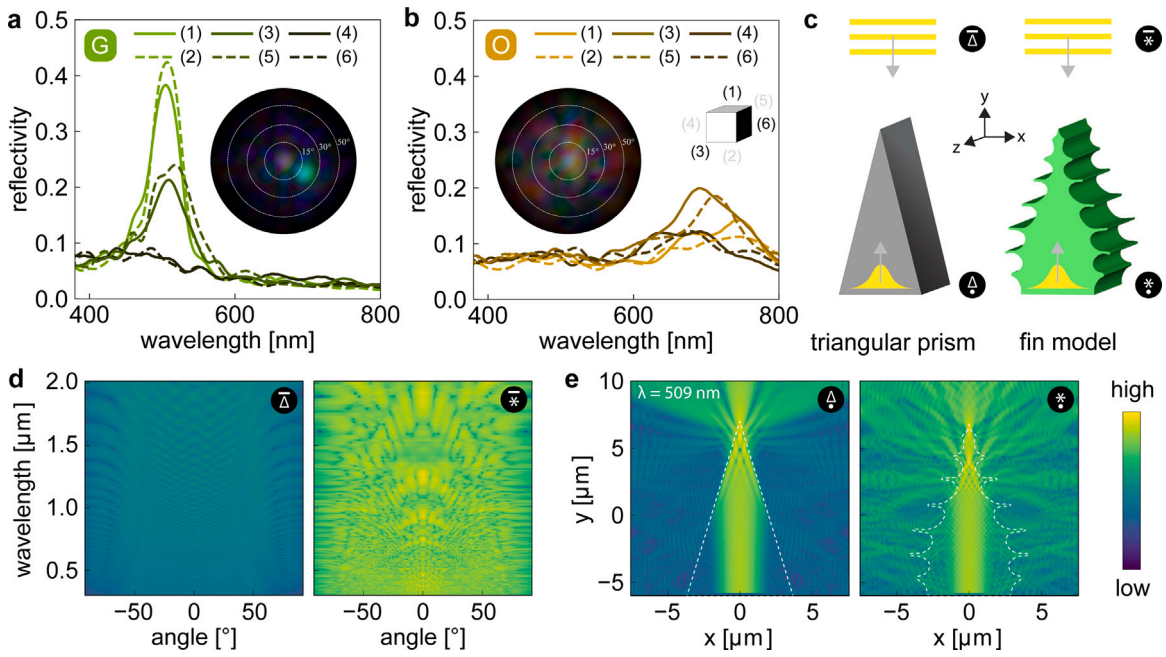

Fig. 6. Full-wave optical simulations of the photonic networks and the cortex. **a,b** Reflectivity of the reconstructed network in a green (a) and orange (b) scale along six directions. The illumination directions are defined in the inset in b: (1) is the scale top surface normal, and (3) the cut-face in the tomography. Gray direction identifiers relate to hidden cube faces. Circular insets are simulated scatterograms based on calculated far-field scattering intensities for 0° polarization. Dashed lines indicate scattering angles 15°, 30° and 50°. **c** Models of the scale's ridged fin, extracted from cross-sectional profiles (right) and simplified to a triangular prism (left). Simulation setting identifiers: white triangle (triangular prism) and star (ridged model) with a horizontal bar on top (plane wave illumination from the top) or a circle below (Gaussian beam illumination from below). **d** Far-field scattering intensity distributions for the triangular prism (left) and the ridge model (right) for 0° polarized plane wave illumination from above. **e** In-plane power distributions for light with wavelength $\lambda = 509\,\mathrm{nm}$ produced by the triangular prism (left) and the ridge model (right), outlined by white dashed lines, for 0° polarized Gaussian beam illumination from below. In d and e, the intensity scales logarithmically, bright areas indicate high intensity, and the absolute range is fixed for each set of images, including the 90° illumination data sets shown in the Supplementary Information. (For interpretation of the references to color in this figure legend, the reader is referred to the web version of this article.)

and then dispersed a fraction to high scattering angles. In contrast, the ridged model (right) scattered light away below the top, visible as intensity streaks in Fig. 6e (right), and weakly focused light at its top. The ridged model thus produced a more homogeneous power distribution than the triangular structure independent of the polarization angle (compare Figure S12).

Our simulations ignored the ~60° inclination of the ridges (compare Materials & Methods), which we expect to cause dominant forward scattering of light from above that could explain the shadowing effect observed in *k*-space of the scale fins.

3. Discussion

This study investigated the physical origin of the non-iridescent, multicolored body pattern of longhorn beetles in the tribe Sternotomini, focusing on *Sternotomis amabilis sylvia*. The colors arise from elytral scales, which combine structural coloration altered by absorbing pigments and feature a distinctive scale geometry with an oblate, bright-appearing scale base, and a vertically extended, ridge-bearing, transparent cortex structure, the fin. Back-focal imaging revealed differences in the scattering behavior of the base and the fin and confirmed a diffusive function of the ridged fins.

Ultrastructural analysis of the scales employed synchrotron USAXS assays, high-resolution FIB-SEM, and synchrotron nanotomography to characterize the photonic nanostructures inside scales and the ridged scale geometry. The green scales were found to contain a polycrystalline network with mostly 8-connected vertices and dominant bond angles of ~70°, ~110° and ~170° (see Fig. 5). Together with the shape of the unit cell (Fig. 5f), these network characteristics are consistent with their identification as an I-WP TPMS-based solid network, similar to the photonic networks found in *Sternotomis callais* beetle scales [15,27]. 2D USAXS data of entire scales further supported the FIB-SEM results and found a polycrystalline network with cubic symmetry. While peak broadening and the ambiguity in the low-index scattering intensity of $Pm\bar{3}m$ and $Im\bar{3}m$ prevented an unambiguous symmetry assignment, synchrotron nanotomography confirmed the I-WP character of the network and underlined the importance of volumetric data sets for analyzing photonic networks with cubic symmetry. Kobayashi et al. pointed toward this pitfall upon their discovery of the I-WP-like network in *S. callais* [15], which contrasted previous assignment of the network to $Pm\bar{3}m$ based on reciprocal USAXS scattering data [19]. With USAXS tomography still being a scarcely accessible technique, our work thus highlights the power of FIB-SEM tomography, particularly as FIB-SEM systems are more readily available, provide higher resolution than currently widely accessible USAXS tomography beamlines, and do not require deconvolution approaches.

In contrast to green scales, orange scales contain a structurally isotropic, quasi-ordered network with an average connectivity $CN_O = (4.9 \pm 0.9)$ and a bond angle distribution with a broad peak at 87°. With a bond angle distribution similar to the amorphous I-WP-like networks in *S. virescens*, this is likely a disordered I-WP-like network with a higher degree of disorder (compare Fig. 6 in [27]).

All scale types are pigmented (Figure S3, Figure S4) and share a common cortex geometry. At the distal scale tip, the cortex forms a triangularly shaped, vertical extension several tens of micrometers high and folded into a chevron pattern of two sets of parallel micrometer-scale ridges fusing at a central ridge. While previous studies on longhorn beetles studied scales that were rather featureless [9,24,27,30,63,64], a similar ridged geometry was described in *S. callais* beetle scales [15] (see Figure 2 and Figure S1 in the Supplementary Material of ref. [15]). The absorbing pigments within the scales act as effective spectral filters of short-wavelength scattered light (Figure S3, Figure S4), similar to what has been seen in numerous butterflies, beetles, and birds [9,26,42,65]. To explore the optical function of the complex scale geometry and understand the interplay of the cortex with the scattering from the photonic networks inside the scales of *S. amabilis sylvia* beetles,

we combined structural and optical modeling of the cortex structures and photonic networks.

In optical simulations, the I-WP-like network in green scales reflected light specularly as predicted for an ordered photonic crystal [50], and the quasi-ordered network in orange scales scattered light angle independently, thus reproducing the general spectral shape and peak characteristics of the experimental results (Fig. 1). The triangularly shaped fin of the scales further alters the scattering of the photonic networks and was found to be an effective diffuser. It is unclear why the ridged structure does not extend over the entire scale surface to suppress the iridescence of the scale base, as in monkey beetles and butterflies [42,66], where the diffusive elements cover nearly the entire scale surface.

Thus, *S. amabilis sylvia* beetles showcase two independent mechanisms toward angle-independent coloration, either through pigmented, isotropic, quasi-ordered photonic networks or polycrystalline networks whose iridescence is suppressed by a superimposed diffusing structure that also features a pigment. The previously studied related beetles *S. callais* [15], *S. mirabilis* [19], *S. pulchra* [19], and *S. virescens* [27] all display angle-independent coloration using a combination of these mechanisms. This study thus broadens our understanding of the diversity of color-producing mechanisms across arthropods [1,19]. It will be interesting to investigate further how insects regulate the interplay of order and disorder to produce both ordered and quasi-ordered photonic networks within the same individual. Such developmental knowledge could unlock the secrets to the facile biomimetic synthesis of designer photonic networks at the visible scales for engineered applications.

4. Conclusion

Sternotomis amabilis sylvia longhorn beetles display a striking non-iridescent pattern of green, orange, and black areas across their bodies. Green and orange colors on the otherwise black elytron arise from colored elongate scales that contain polycrystalline I-WP-like and quasi-ordered photonic networks, respectively. Our work highlights the need for high-resolution volumetric real-space data to accurately diagnose complex 3D nanostructures and the perils of relying on reciprocal scattering data even when coupled with 2D EM images [19,57,67]. By exploring the function of the distinctive scale shape in *S. amabilis sylvia* longhorns, we show that the light reflected by the photonic networks passes through a complex cortex structure, a ridge-bearing fin that suppresses iridescence by acting as a diffuser. The obtained diffusive structural color is further altered by absorbing pigments in the scales, thus creating an angle-independent optical signal across all color patches on the insect. Our study demonstrates that considering the overall scale geometry is crucial for understanding the optical appearance of organisms, an aspect that future studies should consider.

5. Materials and methods

5.1. Specimens

One female and two male, dried, and unmounted specimens of *Sternotomis amabilis sylvia* longhorn beetles were acquired online via etsy.com and ebay.com from insect collectors in France, Europe.

5.2. Integrating sphere spectroscopy

We measured the reflectivity of the specimens with a setup consisting of an integrating sphere connected by two optical fibers (OceanOptics, QP230-2-XSR and OceanOptics, QP450-1-XSR) to a high-power xenon light source (OceanOptics, HPX-2000), and a UV–VIS spectrometer (OceanOptics, Flame-T-XR1-ES), respectively. For normalization, a white diffuser (SphereOptics, Zenith Polymer® SG 3051, 99 %) was used as the reflectance standard, and the dark reference was measured for the open cavity in the integrating sphere. The limited spot size of about 5 mm allowed for measuring several spots in the green and orange areas, while the black stripes were too narrow to avoid overlaps of the measurement spot with differently colored areas. $N = 5$ spectra for each color type were taken and averaged, smoothed with a window length of five and linear interpolation, and plotted using Python. To determine the peak full width at half maximum (FWHM), we used the Python package *lmfit* [68] and fitted the smoothed spectra with a Gaussian distribution on a constant background between 400 nm to 800 nm.

5.3. Optical microscopy

Optical microscopy analysis was performed with an Axio Scope.A1 (Zeiss, Germany) light microscope connected to a xenon-mercury lamp (ThorLabs, SLS400) and custom fitted with an optical fiber attachment for spectral measurements (optical fiber OceanOptics, QP230-1-XRS, spectrometer OceanOptics, QEPRO-VIS-NIR). Images were taken at magnifications of 20 × (Zeiss, EC Epiplan-Aporchromat, NA = 0.6, DH DIC) and 50 × (Zeiss, EC Epiplan-Neofluar, NA = 0.8, DH DIC) with a white diffuser (Labsphere, Spectralon USRS-99-010) as white standard. Scales were imaged directly on the insect or on carbon tape after manual removal. For microspectrophotometry, the white diffuser served as the reflectance standard. A tilted glass slide covered with carbon tape was used as a dark reference, taking into account internal reflections of the microscope optics. Reflectance spectra were recorded from scales on the insect elytron with the 50 × objective. Single-scale transmission spectra were obtained from scales scraped off the insect onto a glass slide.

To quantitatively analyze the scales for pigment content, a refractive index matching oil of $n = 1.55$ was used (Series A; Cargille Laboratories, Cedar Grove, USA). A drop of oil was put on scales on a glass slide, covered with a cover slip, and the transmission spectra repeated with appropriate calibration in an empty region. Spectra were recorded in all measurement modes at 50 × magnification with a measurement spot of about 5 µm in diameter. The spectra were subsequently averaged, smoothed with a window length of five data points and linear interpolation, and plotted using Python. To determine the refractive indices, we calculated the mean absorbance as $A = -\log_{10}(T)$ from the averaged transmittance T of scales immersed in oil ($N = 30$). Following [54], the absorbance was fitted with $D = D_0 \exp(-\lambda/\lambda_0)$, where the resulting $\lambda_{0,G} = 90$ nm and $\lambda_{0,O} = 109$ nm motivated further calculations based on pheomelanin pigmentation [54], an approximation for the pigment in the orange scale. Fitting with $\lambda_0 = \lambda_m = 115$ nm resulted in $D_{0,G} = 3.64$ and $D_{0,O} = 9.43$ used to determine the real refractive index. We calculated the complex refractive indices using effective scale thicknesses of 3.98 µm and 3.00 µm for the green and orange scales, obtained from an estimated 80% of the base width (scales were measured in side view) multiplied by the volume fraction.

For back-focal plane imaging (k-space imaging), the system was color-calibrated with the white diffuser at 100 × (Zeiss, EC Epiplan-Neofluar, NA = 0.9, DH DIC) magnification. A Bertrand lens (Zeiss 453671) was inserted into the light path above the objective at maximally closed field diaphragm, corresponding to a spot diameter of 9.4 µm, so that the plane imaged by the camera would display the signal in Fourier space. The aperture diaphragm was either maximally closed or opened, corresponding to maximal illumination angles of about 15° and 64°, respectively. We analyzed individual scales on carbon tape that were lying upright as on the elytron of the insect.

5.4. Scanning electron microscopy

For scanning electron microscopy, scales were scraped off the insects with single-use needles onto carbon tape and sputtered with 4 nm gold or platinum (Cressington 208HR, United Kingdom) before imaging at 5 kV in a Mira3 LM FE, Tescan (Czech Republic) instrument acquired in 2014. Geometric parameters were measured from SEM images using Fiji [69].

5.5. Focused ion beam sequential cross-sectioning

We used a Scios2, Thermo Fisher Scientific (United States) FIB-SEM dual-beam system to obtain cross-section images from individual scales on carbon tape sputtered with 4 nm gold or platinum. Electron imaging was performed at 5 kV and 0.2 nA, for cutting Ga^+-ion milling currents between 0.5 nA to 3 nA were used at 30 kV ion acceleration voltage. Images recorded at 52° were tilt-corrected accordingly.

FIB-SEM tomography data were recorded automatically with the Auto Slice & View Software (Thermo Fisher Scientific) and reconstructed with Avizo (Thermo Fisher Scientific). The scales used for FIB-SEM tomography were plasma treated at 50 W for 11 min to remove the upper cortex and obtain direct access to the photonic network, and sputtered with 4 nm gold or platinum. Scales with well-visible photonic networks and properly removed cortices were prepared for tomography by backfilling the networks with platinum (Pt) using the electron beam-induced platinum deposition (EBID) at 30 kV and 1.6 nA. Sequential milling of 10 nm thick slices and intermediate SEM imaging produced data with voxel size 10 nm × 10 nm × 10 nm of a cube measuring about 5 μm × 5 μm × 5 μm.

Tomography data were post-processed in Avizo, including cropping, automatic image stack alignment, shear correction, non-local means filtering, binarization, and scaling up by 15% to compensate for uniform shrinkage due to electron beam imaging and plasma treatment. Subvolumes of size 3 μm × 3 μm × 3 μm were extracted for analysis of a direction-dependent reflectivity using FDTD simulations (see below). In orange scales, we observed a uniaxial compression along the Pt-filling direction as blueshifted reflectivity, which we related to the fact that the extracted volume was closer to the Pt-filling face than in green scales. We corrected the observed compression in the data set of the orange scale by additional uniaxial upscaling by 10% along the Pt-filling direction. After artifact-correction, subvolumes of size 3 μm × 3 μm × 3 μm and resulting voxel side length 11.5 nm were extracted and skeletonized in Avizo, producing a skeleton of vertices and struts. This network was corrected for skeletonization artifacts by imposing a minimum strut length of 130 nm using the Fiji plugin BoneITA and corrected for border effects (120 nm) with custom-written Matlab code (see Materials and methods [27]). For visualization, reconstructed volumes were surface smoothed.

5.6. Synchrotron ultra-small-angle X-ray scattering and nanotomography

Individual scales were scraped off the insect elytron onto Kapton® tape. Ultra-small-angle X-ray scattering experiments were conducted in pinhole transmission geometry at the ID02 beamline at the ESRF, Grenoble, with a wavelength of 1 Å, a sample detector distance of 31 m and a spot size of 120 × 50 μm^2. The scattering intensities from the scales were about two orders of magnitude larger than the background from the Kapton® tape and made background subtraction expendable. Following beam stop masking in the software SAXSUtilities, plots of the 2D scattering intensity were obtained in logarithmic scaling, for which values below one were set to unity using Python code. Azimuthal integration of the 2D intensity distributions was performed with SAXSUtilities, while custom-written Python code was used for peak identification, curve normalization, and plotting. For comparison of the 1D scattering curves, the curves were offset manually for better visibility. The low-q slope and primary peak of the 1D scattering curves were fitted in SasView [70] with Porod's law and a Lorentzian, which yielded the peak positions and FWHM for further calculations.

For X-ray nanotomography, individual scales were glued onto insect pins (Entochrysis, Stainless Steel) with two-component epoxy (UHU). Tomography was performed at the P05 imaging beamline, operated by the Helmholtz-Zentrum Hereon at PETRA III (Deutsches Elektronen-Synchrotron (DESY), Hamburg). The measurements were performed at 11 keV using the transmission X-ray microscope with Zernike phase contrast [71,72]. Samples were rotated in the beam, and the projection patterns were processed with Python code (*TomoPy* [73]). The dataset of the orange scale was binned and interactively thresholded in Fiji. Avizo (Thermo Fisher Scientific, v2021.1) was used to binarize and export selected slices. For the dataset of the green scale, denoising was based on a machine learning algorithm [74]. The resulting image stacks with a voxel resolution of 22.8 nm were subjected to histogram equalization in Fiji [69]. Stack alignment, thresholding, and segmentation using a propagating contour algorithm and histogram filtering were again performed in Avizo as well as the final reconstruction.

5.7. 3D modeling of the fin structure

Three-dimensional cortex and fin structure models were created in the open-source 3D modeling software Blender (v. 2.92). The cortex at the base was modeled as a hollow cylinder, compressed and manually edited to approximate the shape and dimensions of the base of orange scales – 240 nm thick, 9 μm wide and 4.9 μm high.

For modeling the scale fin, we filtered and binarized cross-sectional profiles of the fin of a green scale in Avizo and extracted the contours separating the different regions. This line profile was extruded in Blender and superimposed onto a triangular basis of opening angle 7.75°. The structure obtained was symmetrized to approximate the fin shape. To remodel the fin without ridges, a triangular prism with equal height and volume as the scale fin, resulting in a half opening angle of 16.1°, was created directly in the simulation software (see below).

5.8. FDTD simulations

We performed full-wave simulations on the photonic structures in *S. amabilis sylvia* scales using the finite-difference time-domain method in Lumerical (FDTD suite, Ansys, 2023 v. R1.3) as described elsewhere [27,28].

The optical response of the reconstructed photonic networks inside the scales was simulated in three dimensions (3D) with perfectly matched layers (PMLs) as boundaries. The reconstructed networks were assigned the calculated refractive indices for the respective scale type (see Supplementary Information), with the real part ranging from 1.53 to 1.57. The structures were illuminated with a plane wave of 0° or 90° polarization and discretized with a 15 nm mesh size. The results for the reflectivity of the two polarization angles were subsequently averaged to approximate unpolarized illumination. Similarly, the optical response of the base cortex model was simulated in 3D (30 nm mesh size) but assigned a constant refractive index of $n = 1.55$ (without absorption). In an additional simulation, the cortex model was illuminated by a Gaussian beam from below. The source was placed inside the hollow cylinder to mimic the scattering from the photonic networks in the scale lumen.

The scattering behavior of the photonic networks and cortex base model was evaluated by calculating simulated scatterograms from the far-field scattering intensity distributions for 0° polarized plane wave illumination with custom-written Python code using the module *colorscience*. The scatterogram thus obtained is an average of the scattering intensity distributions for all wavelengths between 380 nm to 780 nm weighed with their respective intensity value in the simulated reflectivity spectrum and normalized in the CIE XYZ color space. To approximate the intensity of the experimental k-space images where the limited numerical aperture of the objective captures directional reflections relatively more, the obtained image contrast was then scaled by a factor ×4.

The optical behavior of the fin cortex structure was simulated in two dimensions (2D) with periodic boundary conditions to approximate the scale arrangement on the elytra. The models were assigned a constant refractive index of $n = 1.55$ without absorption. A 15 nm mesh filled the simulation region around the materials, and for the fin models with a 100 nm mesh in the outer areas to minimize computation time. Two illumination settings were used: (i) plane wave illumination from above

the structure and (ii) Gaussian beam illumination from below to mimic the effect of the photonic crystal inside the scale. While the source was placed inside the hollow cylinder for the base mode, it was placed inside the material for the fin models. All simulations were performed for 0° and 90° polarization.

The scattering behavior of the cortex fin models was assessed from 2D far-field scattering intensity distributions and 2D power distributions for light of $\lambda = 509\,\text{nm}$. Intensities were scaled logarithmically, and the shared intensity range was set to the minimum and maximum values for each data set.

Funding

This study was financially supported by the Swiss National Science Foundation and the Adolphe Merkle Foundation, Switzerland. We acknowledge funding from an ERC Advanced Grant PrISMoID, grant number 833895. We are grateful to the European Synchrotron Radiation Facility (ESRF) for supporting this work by granting beamtime, proposal SC5238, and the Helmholtz-Zentrum Hereon and the Deutsches Elektronen-Synchrotron (DESY) with beamtime at the PETRA III imaging beamline P05, proposal I-20191155. I.G. and S.F. gratefully acknowledge financial support from the Deutsche Forschungsgemeinschaft (DFG) (project No. 192346071, SFB 986, project Z2).

CRediT authorship contribution statement

Viola Bauernfeind: Writing – review & editing, Writing – original draft, Visualization, Validation, Methodology, Investigation, Formal analysis, Data curation. **Vinodkumar Saranathan:** Writing – review & editing, Visualization, Validation, Formal analysis, Conceptualization. **Kenza Djeghdi:** Investigation. **Elena Longo:** Resources, Formal analysis. **Silja Flenner:** Software, Formal analysis. **Imke Greving:** Software, Formal analysis. **Ullrich Steiner:** Writing – review & editing, Writing – original draft, Supervision, Funding acquisition, Conceptualization. **Bodo D. Wilts:** Writing – review & editing, Writing – original draft, Supervision, Funding acquisition, Formal analysis, Conceptualization.

Declaration of competing interest

The authors declare that they have no known competing financial interests or personal relationships that could have appeared to influence the work reported in this paper.

Data availability

Data underlying the results presented in this paper are openly available in a Zenodo repository with DOI: 10.5281/zenodo.7568053 [75]. Code is available from the authors upon request.

Acknowledgments

We thank Laureen Matthews from the ESRF for her support during the experiment and for the helpful discussions on the data analysis and Viola Vogler-Neuling for constructive feedback.

Appendix A. Supplementary data

Additional results supporting the findings of this study are available online in the Supplementary Information.

Supplementary material related to this article can be found online at https://doi.org/10.1016/j.mtadv.2024.100524.

References

[1] I.C. Cuthill, W.L. Allen, K. Arbuckle, B. Caspers, G. Chaplin, M.E. Hauber, G.E. Hill, N.G. Jablonski, C.D. Jiggins, A. Kelber, et al., The biology of color, Science 357 (6350) (2017) eaan0221, http://dx.doi.org/10.1126/science.aan0221.

[2] L. Wilkins, D. Osorio, Object colours, material properties and animal signals, J. Exp. Biol. 222 (21) (2019) jeb204487, http://dx.doi.org/10.1242/jeb.204487.

[3] B.D. Wilts, K. Michielsen, J. Kuipers, H. De Raedt, D.G. Stavenga, Brilliant camouflage: photonic crystals in the diamond weevil, *Entimus imperialis*, Proc. R. Soc. B. 279 (1738) (2012) 2524–2530, http://dx.doi.org/10.1098/rspb.2011.2651.

[4] B.D. Wilts, P. Pirih, K. Arikawa, D.G. Stavenga, Shiny wing scales cause spec(tac)ular camouflage of the angled sunbeam butterfly, *Curetis acuta*, Biol. J. Linn. Soc. 109 (2) (2013) 279–289, http://dx.doi.org/10.1111/bij.12070.

[5] H. Fox, G. Vevers, The Nature of Animal Colours, Sidgwick and Jackson Ltd., London, ISBN: 9780283353789, 1960.

[6] D.G. Stavenga, Thin Film and Multilayer Optics Cause Structural Colors of Many Insects and Birds, Mater. Today: Proc. 1 (2014) 109–121, http://dx.doi.org/10.1016/j.matpr.2014.09.007.

[7] E. Shevtsova, C. Hansson, D.H. Janzen, J. Kjærandsen, Stable structural color patterns displayed on transparent insect wings, Proc. Natl. Acad. Sci. 108 (2) (2011) 668–673, http://dx.doi.org/10.1073/pnas.1017393108.

[8] C. Kilchoer, U. Steiner, B.D. Wilts, Thin-film structural coloration from simple fused scales in moths, Interface Focus 9 (2019) 20180044, http://dx.doi.org/10.1098/rsfs.2018.0044.

[9] E. Bermúdez-Ureña, C. Kilchoer, N.P. Lord, U. Steiner, B.D. Wilts, Structural Diversity with Varying Disorder Enables the Multicolored Display in the Longhorn Beetle *Sulawesiella rafaelae*, iScience 23 (7) (2020) 101339, http://dx.doi.org/10.1016/j.isci.2020.101339.

[10] M. Jacobs, M. Lopez-Garcia, O. Phrathep, T. Lawson, R. Oulton, H.M. Whitney, et al., Photonic multilayer structure of *Begonia* chloroplasts enhances photosynthetic efficiency, Nat. Plants 2 (11) (2016) 1–6, http://dx.doi.org/10.1038/nplants.2016.162.

[11] H. Whitney, M. Kolle, R. Alvarez-Fernandez, U. Steiner, B. Glover, Contributions of iridescence to floral patterning, Commun. Integr. Biol. 2 (3) (2009) 230–232, http://dx.doi.org/10.4161/cib.2.3.8084.

[12] S. Vignolini, E. Moyroud, T. Hingant, H. Banks, P.J. Rudall, U. Steiner, B.J. Glover, The flower of *Hibiscus trionum* is both visibly and measurably iridescent, New Phytol. 205 (1) (2015) 97–101, http://dx.doi.org/10.1111/nph.12958.

[13] X. Fan, X. Zheng, T. An, X. Li, N. Leung, B. Zhu, T. Sui, N. Shi, T. Fan, Q. Zhao, Light diffraction by sarcomeres produces iridescence in transmission in the transparent ghost catfish, Proc. Natl. Acad. Sci. 120 (12) (2023) e2219300120, http://dx.doi.org/10.1073/pnas.2219300120.

[14] K. Michielsen, D.G. Stavenga, Gyroid cuticular structures in butterfly wing scales: biological photonic crystals, J. R. Soc. Interface 5 (18) (2008) 85–94, http://dx.doi.org/10.1098/rsif.2007.1065.

[15] Y. Kobayashi, R. Ohnuki, S. Yoshioka, Discovery of I-WP minimal-surface-based photonic crystal in the scale of a longhorn beetle, J. R. Soc. Interface 18 (184) (2021) 20210505, http://dx.doi.org/10.1098/rsif.2021.0505.

[16] K. Edagawa, S. Kanoko, M. Notomi, Photonic Amorphous Diamond Structure with a 3D Photonic Band Gap, Phys. Rev. Lett. 100 (1) (2008) 013901, http://dx.doi.org/10.1103/PhysRevLett.100.013901.

[17] J.D. Joannopoulos, S.G. Johnson, J.N. Winn, R.D. Meade, Photonic Crystals: Molding the Flow of Light (Second Edition), Princeton Univ. Press, Princeton, NJ, 2008, http://dx.doi.org/10.1515/9781400828241.

[18] V. Saranathan, C.O. Osuji, S.G. Mochrie, H. Noh, S. Narayanan, A. Sandy, E.R. Dufresne, R.O. Prum, Structure, function, and self-assembly of single network gyroid ($I4_132$) photonic crystals in butterfly wing scales, Proc. Natl. Acad. Sci. 107 (26) (2010) 11676–11681, http://dx.doi.org/10.1073/pnas.0909616107.

[19] V. Saranathan, A.E. Seago, A. Sandy, S. Narayanan, S.G. Mochrie, E.R. Dufresne, H. Cao, C.O. Osuji, R.O. Prum, Structural Diversity of Arthropod Biophotonic Nanostructures Spans Amphiphilic Phase-Space, Nano Lett. 15 (6) (2015) 3735–3742, http://dx.doi.org/10.1021/acs.nanolett.5b00201.

[20] A.E. Seago, P. Brady, J.-P. Vigneron, T.D. Schultz, Gold bugs and beyond: a review of iridescence and structural colour mechanisms in beetles (Coleoptera), J. R. Soc. Interface 6 (2009) S165–S184, http://dx.doi.org/10.1098/rsif.2008.0354.focus.

[21] S. Kinoshita, S. Yoshioka, J. Miyazaki, Physics of structural colors, Rep. Progr. Phys. 71 (7) (2008) 076401, http://dx.doi.org/10.1088/0034-4885/71/7/076401.

[22] P. Vukusic, J.R. Sambles, Photonic structures in biology, Nature 424 (6950) (2003) 852–855, http://dx.doi.org/10.1038/nature01941.

[23] B.D. Wilts, J. Otto, D.G. Stavenga, Ultra-dense, curved, grating optics determines peacock spider coloration, Nanoscale Adv. 2 (3) (2020) 1122–1127, http://dx.doi.org/10.1039/C9NA00494G.

[24] E. Van Hooijdonk, C. Barthou, J.P. Vigneron, S. Berthier, Yellow structurally modified fluorescence in the longhorn beetles *Celosterna pollinosa sulfurea* and *Phosphorus virescens* (Cerambycidae), J. Lumin. 136 (2013) 313–321, http://dx.doi.org/10.1016/j.jlumin.2012.12.022.

[25] S. Yoshioka, S. Kinoshita, Effect of Macroscopic Structure in Iridescent Color of the Peacock Feathers, FORMA 17 (2) (2002) 169–181.

[26] M.D. Shawkey, L. D'Alba, Interactions between colour-producing mechanisms and their effects on the integumentary colour palette, Phil. Trans. R. Soc. B 372 (1724) (2017) 20160536, http://dx.doi.org/10.1098/rstb.2016.0536.

[27] V. Bauernfeind, K. Djeghdi, I. Gunkel, U. Steiner, B.D. Wilts, Photonic Amorphous I-WP-Like Networks Create Angle-Independent Colors in *Sternotomis virescens* Longhorn Beetles, Adv. Funct. Mater. 34 (35) (2024) 2302720, http://dx.doi.org/10.1002/adfm.202302720.

[28] K. Djeghdi, U. Steiner, B.D. Wilts, 3D Tomographic Analysis of the Order-Disorder Interplay in the *Pachyrhynchus congestus mirabilis* Weevil, Adv. Sci. 9 (26) (2022) 2202145, http://dx.doi.org/10.1002/advs.202202145.

[29] A. Parisotto, U. Steiner, A.A. Cabras, M.H. Van Dam, B.D. Wilts, *Pachyrhynchus* Weevils Use 3D Photonic Crystals with Varying Degrees of Order to Create Diverse and Brilliant Displays, Small 18 (20) (2022) 2200592, http://dx.doi.org/10.1002/smll.202200592.

[30] B. Dong, T. Zhan, X. Liu, L. Jiang, F. Liu, X. Hu, J. Zi, Optical response of a disordered bicontinuous macroporous structure in the longhorn beetle *Sphingnotus mirabilis*, Phys. Rev. E 84 (1) (2011) 011915, http://dx.doi.org/10.1103/PhysRevE.84.011915.

[31] E. Moyroud, T. Wenzel, R. Middleton, P.J. Rudall, H. Banks, A. Reed, G. Mellers, P. Killoran, M.M. Westwood, U. Steiner, et al., Disorder in convergent floral nanostructures enhances signalling to bees, Nature 550 (7677) (2017) 469–474, http://dx.doi.org/10.1038/nature24285.

[32] M. Rothammer, C. Zollfrank, K. Busch, G. von Freymann, Tailored Disorder in Photonics: Learning from Nature, Adv. Opt. Mater. 9 (19) (2021) 2100787, http://dx.doi.org/10.1002/adom.202100787.

[33] L. Shi, Y. Zhang, B. Dong, T. Zhan, X. Liu, J. Zi, Amorphous Photonic Crystals with Only Short-Range Order, Adv. Mater. 25 (37) (2013) 5314–5320, http://dx.doi.org/10.1002/adma.201301909.

[34] S.R. Sellers, W. Man, S. Sahba, M. Florescu, Local self-uniformity in photonic networks, Nat. Commun. 8 (2017) 14439, http://dx.doi.org/10.1038/ncomms14439.

[35] D.S. Wiersma, Disordered photonics, Nat. Photonics 7 (3) (2013) 188–196, http://dx.doi.org/10.1038/nphoton.2013.29.

[36] S. Yu, C.-W. Qiu, Y. Chong, S. Torquato, N. Park, Engineered disorder in photonics, Nat. Rev. Mater. 6 (3) (2021) 226–243, http://dx.doi.org/10.1038/s41578-020-00263-y.

[37] S.M. Doucet, M.G. Meadows, Iridescence: a functional perspective, J. R. Soc. Interface 6 (2009) S115–S132, http://dx.doi.org/10.1098/rsif.2008.0395.focus.

[38] K. Kjernsmo, H.M. Whitney, N.E. Scott-Samuel, J.R. Hall, H. Knowles, L. Talas, I.C. Cuthill, Iridescence as Camouflage, Curr. Biol. 30 (3) (2020) 551–555, http://dx.doi.org/10.1016/j.cub.2019.12.013.

[39] D.J. Kemp, Female mating biases for bright ultraviolet iridescence in the butterfly *Eurema hecabe* (Pieridae), Behav. Ecol. 19 (1) (2008) 1–8, http://dx.doi.org/10.1093/beheco/arm094.

[40] L.T. McDonald, S. Narayanan, A. Sandy, V. Saranathan, M.E. McNamara, Brilliant angle-independent structural colours preserved in weevil scales from the Swiss Pleistocene, Biol. Lett. 16 (4) (2020) 20200063, http://dx.doi.org/10.1098/rsbl.2020.0063.

[41] B.D. Wilts, N. IJbema, D.G. Stavenga, Pigmentary and photonic coloration mechanisms reveal taxonomic relationships of the Cattlehearts (Lepidoptera: Papilionidae: *Parides*), BMC Evol. Biol. 14 (2014) 1–11, http://dx.doi.org/10.1186/s12862-014-0160-9.

[42] C. Kilchoer, P. Pirih, U. Steiner, B.D. Wilts, Diffusive structural colour in *Hoplia argentea*, J. Exp. Biol. 222 (24) (2019) jeb213306, http://dx.doi.org/10.1242/jeb.213306.

[43] R.A. Haack, Feeding Biology of Cerambycids, in: Q. Wang (Ed.), Cerambycidae of the World; Biology and Pest Management, CRC Press, Boca Raton, ISBN: 9781315313252, 2017, pp. 105–124, http://dx.doi.org/10.1201/b21851.

[44] A. Slipinski, H. Escalona, Australian Longhorn Beetles (Coleoptera: Cerambycidae) Volume 1: Introduction and Subfamily Lamiinae, CSIRO Publishing, Collingwood, ISBN: 9781486300037, 2013.

[45] V. Allard, Les Coléoptères du Monde: Sternotomini, Sciences Nat, Paris, 1993, p. 111.

[46] D. de Santana Souza, L. Marinoni, M.L. Monné, J. Gómez-Zurita, Molecular phylogenetic assessment of the tribal classification of Lamiinae (Coleoptera: Cerambycidae), Mol. Phylogenet. Evo. 145 (2020) 106736, http://dx.doi.org/10.1016/j.ympev.2020.106736.

[47] L. Han, S. Che, An Overview of Materials with Triply Periodic Minimal Surfaces and Related Geometry: From Biological Structures to Self-Assembled Systems, Adv. Mater. 30 (17) (2018) 1705708, http://dx.doi.org/10.1002/adma.201705708.

[48] B.D. Wilts, P.L. Clode, N.H. Patel, G.E. Schröder-Turk, Nature's functional nanomaterials: Growth or self-assembly? MRS Bull. 44 (2) (2019) 106–112, http://dx.doi.org/10.1557/mrs.2019.21.

[49] B.D. Wilts, B. Apeleo Zubiri, M.A. Klatt, B. Butz, M.G. Fischer, S.T. Kelly, E. Spiecker, U. Steiner, G.E. Schröder-Turk, Butterfly gyroid nanostructures as a time-frozen glimpse of intracellular membrane development, Sci. Adv. 3 (4) (2017) e1603119, http://dx.doi.org/10.1126/sciadv.1603119.

[50] R. Ohnuki, Y. Kobayashi, S. Yoshioka, Polarization-dependent reflection of I-WP minimal-surface-based photonic crystal, Phys. Rev. E 106 (1) (2022) 014123, http://dx.doi.org/10.1103/PhysRevE.106.014123.

[51] R. Galant, J.B. Skeath, S. Paddock, D.L. Lewis, S.B. Carroll, Expression pattern of a butterfly *achaete-scute* homolog reveals the homology of butterfly wing scales and insect sensory bristles, Curr. Biol. 8 (14) (1998) 807–813, http://dx.doi.org/10.1016/S0960-9822(98)70322-7.

[52] M. Srinivasarao, Nano-Optics in the Biological World: Beetles, Butterflies, birds, and moths, Chem. Rev. 99 (7) (1999) 1935–1962, http://dx.doi.org/10.1021/cr970080y.

[53] H.L. Leertouwer, B.D. Wilts, D.G. Stavenga, Refractive index and dispersion of butterfly chitin and bird keratin measured by polarizing interference microscopy, Opt. Express 19 (24) (2011) 24061–24066, http://dx.doi.org/10.1364/OE.19.024061.

[54] D.G. Stavenga, H.L. Leertouwer, T. Hariyama, H.A. De Raedt, B.D. Wilts, Sexual Dichromatism of the Damselfly *Calopteryx japonica* Caused by a Melanin-Chitin Multilayer in the Male Wing Veins, PLOS ONE 7 (11) (2012) e49743, http://dx.doi.org/10.1371/journal.pone.0049743.

[55] P. Vukusic, D. Stavenga, Physical methods for investigating structural colours in biological systems, J. R. Soc. Interface 6 (2009) S133–S148, http://dx.doi.org/10.1098/rsif.2008.0386.focus.

[56] D. Stavenga, H. Leertouwer, P. Pirih, M. Wehling, Imaging scatterometry of butterfly wing scales, Opt. Express 17 (2009) 193–202, http://dx.doi.org/10.1364/OE.17.000193.

[57] A.C. Finnefrock, R. Ulrich, G.E. Toombes, S.M. Gruner, U. Wiesner, The Plumber's Nightmare:[1] A New Morphology in Block Copolymer-Ceramic Nanocomposites and Mesoporous Aluminosilicates, J. Am. Chem. Soc. 125 (43) (2003) 13084–13093, http://dx.doi.org/10.1021/ja0355170.

[58] V. Saranathan, J.D. Forster, H. Noh, S.-F. Liew, S.G. Mochrie, H. Cao, E.R. Dufresne, R.O. Prum, Structure and optical function of amorphous photonic nanostructures from avian feather barbs: a comparative small angle X-ray scattering (SAXS) analysis of 230 bird species, J. R. Soc. Interface 9 (75) (2012) 2563–2580, http://dx.doi.org/10.1098/rsif.2012.0191.

[59] V. Saranathan, S. Narayanan, A. Sandy, E.R. Dufresne, R.O. Prum, Evolution of single gyroid photonic crystals in bird feathers, Proc. Natl. Acad. Sci. 118 (23) (2021) e2101357118, http://dx.doi.org/10.1073/pnas.2101357118.

[60] M. Maldovan, E.L. Thomas, Diamond-structured photonic crystals, Nature Mater. 3 (9) (2004) 593–600, http://dx.doi.org/10.1038/nmat1201.

[61] B.D. Wilts, V. Saranathan, A Literal Elytral Rainbow: Tunable Structural Colors Using Single Diamond Biophotonic Crystals in *Pachyrrhynchus congestus* Weevils, Small 14 (46) (2018) 1802328, http://dx.doi.org/10.1002/smll.201802328.

[62] V. Saranathan, Topology of Minimal Surface Biophotonic Nanostructures in Arthropods, in: S. Gupta, A. Saxena (Eds.), The Role of Topology in Materials, Springer International Publishing, Cham, ISBN: 9783319765952, 2018, pp. 275–290, http://dx.doi.org/10.1007/978-3-319-76596-9_11.

[63] P. Simonis, J.P. Vigneron, Structural color produced by a three-dimensional photonic polycrystal in the scales of a longhorn beetle: *Pseudomyagrus waterhousei* (Coleoptera: Cerambicidae), Phys. Rev. E 83 (1) (2011) 011908, http://dx.doi.org/10.1103/PhysRevE.83.011908.

[64] J.-F. Colomer, P. Simonis, A. Bay, P. Cloetens, H. Suhonen, M. Rassart, C. Vandenbem, J.P. Vigneron, Photonic polycrystal in the greenish-white scales of the African longhorn beetle *Prosopocera lactator* (Cerambycidae), Phys. Rev. E 85 (1) (2012) 011907, http://dx.doi.org/10.1103/PhysRevE.85.011907.

[65] B.D. Wilts, A. Matsushita, K. Arikawa, D.G. Stavenga, Spectrally tuned structural and pigmentary coloration of birdwing butterfly wing scales, J. R. Soc. Interface 12 (111) (2015) 20150717, http://dx.doi.org/10.1098/rsif.2015.0717.

[66] B.D. Wilts, K. Michielsen, H. De Raedt, D.G. Stavenga, Iridescence and spectral filtering of the gyroid-type photonic crystals in *Parides sesostris* wing scales, Interface Focus 2 (5) (2012) 681–687, http://dx.doi.org/10.1098/rsfs.2011.0082.

[67] G.E. Toombes, A.C. Finnefrock, M.W. Tate, R. Ulrich, U. Wiesner, S.M. Gruner, A Re-Evaluation of the Morphology of a Bicontinuous Block Copolymer-Ceramic Material, Macromolecules 40 (25) (2007) 8974–8982, http://dx.doi.org/10.1021/ma0715369.

[68] M. Newville, T. Stensitzki, D.B. Allen, A. Ingargiola, LMFIT: Non-Linear Least-Square Minimization and Curve-Fitting for Python, Zenodo, 2015, http://dx.doi.org/10.5281/zenodo.11813.

[69] J. Schindelin, I. Arganda-Carreras, E. Frise, V. Kaynig, M. Longair, T. Pietzsch, S. Preibisch, C. Rueden, S. Saalfeld, B. Schmid, et al., Fiji: an open-source platform for biological-image analysis, Nat. Methods 9 (7) (2012) 676–682, http://dx.doi.org/10.1038/nmeth.2019.

[70] M. Doucet, J.H. Cho, G. Alina, Z. Attala, J. Bakker, W. Bouwman, P. Butler, K. Campbell, T. Cooper-Benun, C. Durniak, L. Forster, M. Gonzales, R. Heenan, A. Jackson, S. King, P. Kienzle, J. Krzywon, T. Nielsen, L. O'Driscoll, W. Potrzebowski, S. Prescott, R. Ferraz Leal, P. Rozycko, T. Snow, A. Washington, SasView Version 5.0.3, Zenodo, 2020, http://dx.doi.org/10.5281/zenodo.3930098.

[71] S. Flenner, M. Storm, A. Kubec, E. Longo, F. Döring, D.M. Pelt, C. David, M. Müller, I. Greving, Pushing the temporal resolution in absorption and Zernike phase contrast nanotomography: enabling fast *in situ* experiments, J. Synchrotron Radiat. 27 (5) (2020) 1339–1346, http://dx.doi.org/10.1107/S1600577520007407.

[72] S. Flenner, J. Hagemann, M. Storm, A. Kubec, P. Qi, C. David, E. Longo, S. Niese, P. Gawlitza, B. Zeller-Plumhoff, et al., Hard X-ray nanotomography at the P05 imaging beamline at PETRA III, in: B. Müller, G. Wang (Eds.), Developments in X-Ray Tomography XIV, vol. 12242, SPIE, 2022, pp. 107–114, http://dx.doi.org/10.1117/12.2632706.

[73] D. Gürsoy, F. De Carlo, X. Xiao, C. Jacobsen, TomoPy: a framework for the analysis of synchrotron tomographic data, J. Synchrotron Radiat. 21 (5) (2014) 1188–1193, http://dx.doi.org/10.1107/S1600577514013939.

[74] S. Flenner, S. Bruns, E. Longo, A.J. Parnell, K.E. Stockhausen, M. Müller, I. Greving, Machine learning denoising of high-resolution X-ray nanotomography data, J. Synchrotron Radiat. 29 (2022) 230–238, http://dx.doi.org/10.1107/S1600577521011139.

[75] V. Bauernfeind, V. Saranathan, K. Djeghdi, E. Longo, S. Flenner, I. Greving, U. Steiner, B.D. Wilts, Supporting Dataset, Zenodo, 2024, http://dx.doi.org/10.5281/zenodo.7568053.